IET Electric Power Applications

Research Article

IET Journals
The Institution of Engineering and Technology

Eccentric position diagnosis of static eccentricity fault of external rotor permanent magnet synchronous motor as an in-wheel motor

ISSN 1751-8660
Received on 22nd July 2019
Revised 6th April 2020
Accepted on 21st July 2020
E-First on 2nd September 2020
doi: 10.1049/iet-epa.2019.0617
www.ietdl.org

Conggan Ma[1,2], Yujiao Gao[1], Michele Degano[2] ✉, Yanyan Wang[1], Jianguang Fang[3], Christopher Gerada[2], Shengsen Zhou[1], Yuanye Mu[1]

[1]*School of Automotive Engineering, Harbin Institute of Technology-Weihai, Weihai, People's Republic of China*
[2]*Department of Electrical and Electronic Engineering, The University of Nottingham, Nottingham, UK*
[3]*School of Civil and Environmental Engineering, University of Technology Sydney, Sydney, Australia*
✉ *E-mail: Michele.Degano@nottingham.ac.uk*

Abstract: An eccentric position diagnosis method of static eccentricity (SE) fault of external rotor permanent magnet synchronous motor (ER-PMSM) is presented. Firstly, an analytical model of no-load radial magnetic field of ER-PMSM is established. Analytical models of no-load Back-EMF of both unit motors and the whole motor are carried out and are verified by finite element method (FEM) and experimental measurements. Then, the influences of SE ratio, SE circumferential angle, winding distribution mode and number of parallel branches on no-load radial magnetic field and no-load Back-EMF are analyzed based on these analytical models. The results show that SE does not affect the frequency characteristics of no-load radial magnetic field, but changes space order characteristics. On one hand, for ER-PMSM, of which the number of unit motors is equal to 1, SE causes no-load Back-EMF distortion. On the other hand, for ER-PMSM, of which the number of unit motors is greater than 1, SE does not affect no-load Back-EMF of the whole motor, but it still leads to no-load Back-EMF distortion of unit motors. Therefore, based on total harmonic distortion (THD) of no-load Back-EMF of unit motor, a projection method of intersection lines for SE fault diagnosis of ER-PMSM is proposed finally.

1 Introduction

As a direct driving motor of electric vehicles, the in-wheel motor is energy-efficient and environment-protective [1]. External rotor permanent magnet synchronous motor (ER-PMSM) has gradually become one of the main in-wheel motors with the characteristics of low loss, simple and compact structure, reliable operation, and high efficiency. Therefore, research on ER-PMSM as an in-wheel motor is gaining more interest. However, during its actual operation, eccentricity faults may occur due to manufacturing tolerances, bearing wear, or complex road excitation especially. As a result, the length of the air gap of ER-PMSM changes, and the distribution of the air gap magnetic field becomes uneven. The uneven air gap magnetic field leads to the distortion of the back electromotive force (back-EMF) further. Then, harmonic components of back-EMF cause electromagnetic torque pulsation further, which reduces motor performance. Static eccentricity (SE) is present in most cases after ER-PMSM is manufactured. Therefore, it is of great significance to study and diagnose SE of ER-PMSM as an in-wheel motor.

No-load back-EMF is an important parameter in the motor design process, which is usually used to evaluate the rationality of the motor design. The calculation of no-load back-EMF is based on an accurate solution of the no-load air gap magnetic field. Accordingly, no-load back-EMF can also be used to verify the accuracy of the analytical model of the air gap magnetic field. The solution methods of air gap magnetic field can be divided into analytical methods and finite-element methods (FEMs) mainly. Analytical methods mainly include the subdomain method [2–10] and the magnetic potential permeance method [11, 12]. No-load back-EMF is generally solved through the Faraday's law of electromagnetic induction or FEM. Zhu *et al.* calculated the air gap magnetic field of the slotted motor with different pole–slot combinations, thereby improving the calculation accuracy of cogging torque with relatively large slot opening width [4]. Rahideh and Korakianitis calculated the magnetic field distribution of the permanent magnet (PM) motor in six magnetisation modes by using of subdomain method and verified it through FEM [5]. Zhou *et al.* used a subdomain method to calculate the air gap magnetic field of a surface-mounted PM motor with different PM shapes and verified the analytical model with FEM [10]. Zarko *et al.* calculated the air gap magnetic field of surface-mounted PM motor by using complex relative permeance considering radial and parallel magnetisation modes meanwhile [11]. In [12], the air gap magnetic field in the stator static coordinate and the rotor motion coordinate were both calculated, respectively, by the magnetic potential permeance method. Park *et al.* used the field reconstruction method to calculate the air gap magnetic field of axial flux motor with skewed PM, which reduced a computational burden significantly [13]. Rahideh *et al.* calculated the no-load magnetic field and armature reactive magnetic field under three magnetisation modes, and analysed the influence of three magnetisation modes on back-EMF [14, 15]. Kim and Lieu [16, 17] used the perturbation method to consider the magnetic field distribution of PM motor with rotor eccentricity under the condition of slotless and slotted, respectively. Jalali *et al.* developed an approach to model the air gap flux density of surface-mounted PM motor under eccentricity through the equivalent boundary method [18]. In [19], the no-load magnetic field under static, dynamic, and mixed eccentricity of slotless brushless PM motor were analysed and calculated. The results showed that rotor eccentricity had a certain influence on the radial and tangential components of the air gap magnetic field, but no influence on the back-EMF waveforms [19]. In [20], the influences of different pole/slot combinations and winding configurations on the performance of PM motor with rotor eccentricity were investigated. The results showed that the rotor eccentricity did not affect the back-EMF and electromagnetic torque of the rotary symmetric motor, but seriously distorted the back-EMF and torque waveforms of rotary asymmetric motor [20]. Zheng *et al.* analysed the influence of magnetic saturation and rotor eccentricity on back-EMF of a novel hybrid-excited stator slot opening PM machine

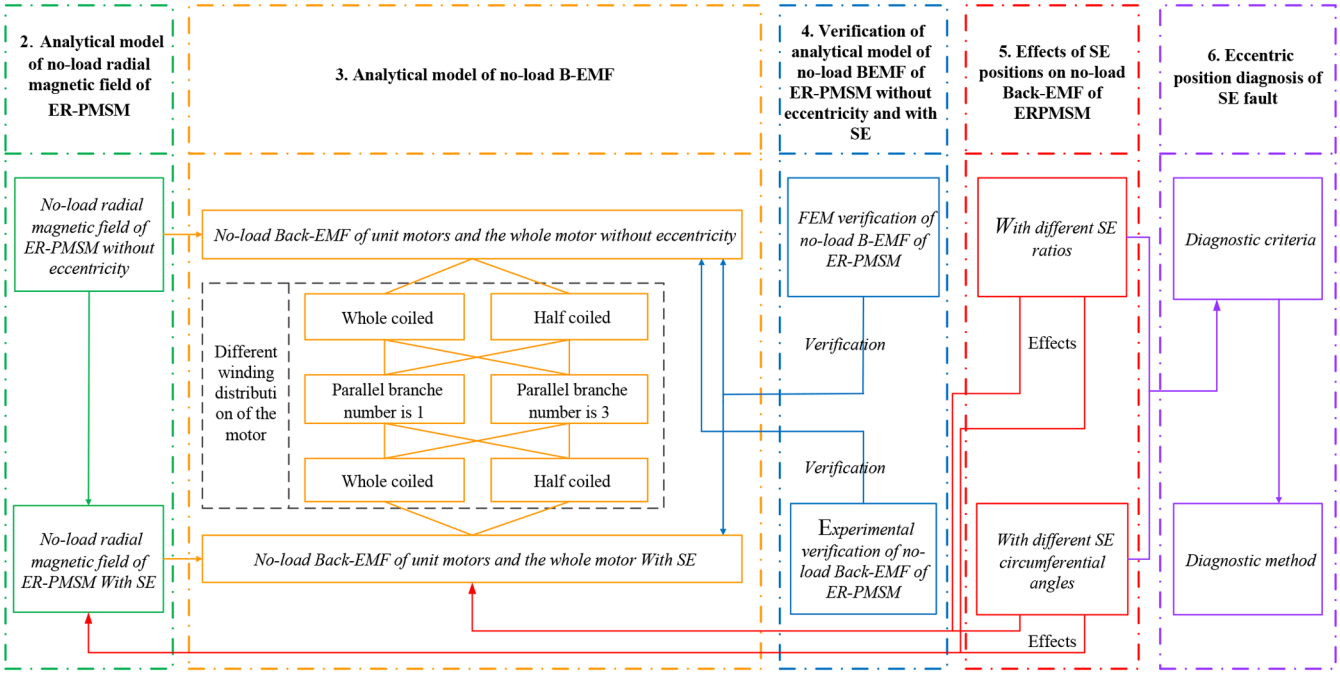

Fig. 1 *Overall structure of this paper*

through FEM and verified it through experiments [21]. Ebrahimi *et al.* proposed a method to diagnose motor eccentricity by taking the amplitudes of sideband components with a particular frequency pattern, which were extracted from the spectrum of stator current as of the index [22]. This method can distinguish the eccentric forms. Hassanzadeh *et al.* also diagnosed different eccentric forms through the frequency characteristics analysis of currents in [23, 24]. Kang *et al.* added additional windings to a motor, and then detected dynamic eccentricity by measuring back-EMF in the additional windings [25]. This method can be applied to the operating conditions of stationary and non-stationary rotational speeds. Park *et al.* added hall sensors inside the motor and then diagnosed static, dynamic, and mixed eccentricity through flux changes in different directions [26]. Dorrell and Salah [27] determined the eccentricity degree by measuring the induced voltage of the induction coil attached to the wound rotor induction motors.

However, some deficiencies still exist:

(i) The influences of some important design parameters such as winding distribution modes and the number of parallel branches on back-EMF are ignored.
(ii) The effects of the SE ratio on the air gap magnetic field and back-EMF have been revealed already. However, the effects of SE circumferential angles, which distort the air gap magnetic field and back-EMF severely, are always neglected.
(iii) Most of the eccentric diagnosis methods can only be realised through complicated post-processing of measurement data in [18–21] or additional devices in [22–24]. As a result, the eccentricity fault cannot be diagnosed quickly or directly or at a low cost. Additionally, only the SE ratio can be detected but not the important SE circumferential angle.

In addition, in [28], the effects of SE fault on no-load back-EMF of external rotor PM DC brushless motor with 46 poles and 51 slots are discussed. However, there are three areas for improvement in [28]:

(i) In [28], the number of unit motors of external rotor PM DC brushless motor is equal to 1, so the effects of SE fault on no-load back-EMF is only applicable to the motor with 1 unit motor. When the number of unit motors is >1, the asymmetry of three-phase no-load back-EMF of a single unit motor will be offset due to the series and parallel connections of multiple unit motors. Therefore, the law revealed in [28] is not applicable to SE fault diagnosis of the motor with a unit motor number >1.
(ii) The authors of [28] only studied the effects of the SE ratio on no-load back-EMF, ignoring the effects caused by SE circumferential angle. Nevertheless, SE circumferential angle will also significantly cause the asymmetry of three-phase no-load back-EMF.
(iii) Only no-load back-EMF under one winding distribution form was analysed in [28], the influences of parallel branch numbers and winding connection modes on no-load back-EMF were ignored. However, for the motor with SE fault, the asymmetry of three-phase no-load back-EMF will be greatly affected by different parallel branch numbers and different winding connection modes.

Therefore, the effects of different SE ratios and SE circumferential angles on the no-load radial magnetic field and no-load back-EMF of ER-PMSM are discussed in this paper, taking into account different winding distribution modes and different numbers of parallel branches. The space order characteristics and frequency characteristics of the no-load radial magnetic field are revealed by two-dimensional Fourier transform. Based on the influence analysis of SE on no-load back-EMF, an eccentric position including SE ratio and SE circumferential angle is detected accurately. This is carried out for a unit motor and the whole motor, where the unit motor is defined as a portion of motor presenting the greatest common divisor (GCD) of pole pairs and slots number. A 24-pole-27-slot ER-PMSM used as an in-wheel motor is considered as a case study to illustrate the proposed method. The whole paper includes seven sections, and the overall structure is shown in Fig. 1.

2 Analytical model of no-load radial magnetic field of ER-PMSM

2.1 No-load radial magnetic field of ER-PMSM without eccentricity

It is assumed that PMs are magnetised radially, the magnetisation intensity within the section of PMs is uniform, and the permeability of iron core is infinite. No-load magnetic field is calculated by the equivalent remanence method in polar coordinates, and no-load radial magnetic field considering the slotting effect is obtained by using of the complex relative permeance method.

The formula of the no-load radial magnetic field considering slotting effect of ER-PMSM is [10]

$$B_{r}(\theta,r,t)=B_{r-s}(\theta,r,t)\lambda_a(\theta)+B_{t-s}(\theta,r,t)\lambda_b(\theta)$$
$$=\left\{\sum_{k=1,3,5,\ldots}^{\infty}B_{r-s\_amp\_k}(r)\times\cos[kp(\theta-\omega t-\theta_0)]\right\}\lambda_a(\theta)$$
$$+\left\{\sum_{k=1,3,5,\ldots}^{\infty}B_{t-s\_amp\_k}(r)\times\sin[kp(\theta-\omega t-\theta_0)]\right\}\lambda_b(\theta) \quad (1)$$

where B_{r-s} and B_{t-s} are the no-load radial and tangential magnetic fields without considering slotting effect, respectively, λ_a and $\lambda_b$are the real and imaginary part of the complex relative permeance, ω is the motor speed (rad/s), and θ_0 is the initial position of the rotor.

The real and imaginary part of the complex relative permeance can be expressed as the following Fourier series forms [9]:

$$\begin{cases}\lambda_a(\theta)=\lambda_0+\sum_{\eta=1}^{N_\lambda}\lambda_{a\eta}\cos(\eta Q_s\theta)\\ \lambda_b(\theta)=\sum_{\eta=1}^{N_\lambda}\lambda_{b\eta}\sin(\eta Q_s\theta)\end{cases} \quad (2)$$

where N_λ is the largest order of the Fourier coefficient and Q_s is the number of slots.

2.2 No-load radial magnetic field of ER-PMSM with SE

If SE occurs, the relative position of the stator and rotor of the motor can be determined through the SE distance e and the SE circumferential angle γ in Fig. 2.

The SE ratio can be expressed as

$$\xi=\frac{e}{\delta_0}\times 100\% \quad (3)$$

where δ_0 is the length of the uniform air gap.

In this paper, the SE ratio and SE circumferential angle are considered concurrently. The permeance correction coefficient of SE is defined as

$$\varepsilon_s(\varepsilon,\gamma)=\varepsilon_0+\varepsilon_1\cos(\theta-\gamma)$$
$$=\frac{1}{\sqrt{1-\varepsilon^2}}+\frac{2}{\sqrt{1-\varepsilon^2}}\cdot\frac{1-\sqrt{1-\varepsilon^2}}{\varepsilon}\cdot\cos(\theta-\gamma) \quad (4)$$

where ε is the effective SE ratio, $\varepsilon=e/(\delta_0+\delta')$, $\delta'=h_{PM}/(\mu_r)$, h_{PM} is the PM thickness, and μ_r is the relative permeability.

The no-load radial magnetic field of ER-PMSM with SE can be obtained by multiplying no-load radial magnetic field without eccentricity and the magnetic permeance correction coefficient of SE

$$B_{r-se}(\theta,r,t)=B_r(\theta,r,t)\cdot\varepsilon_s(\varepsilon,\gamma)$$
$$=\begin{bmatrix}B_{r-s}(\theta,r,t)\times\lambda_a(\theta)\\ +B_{t-s}(\theta,r,t)\times\lambda_b(\theta)\end{bmatrix}\times[\varepsilon_0+\varepsilon_1\cos(\theta-\gamma)] \quad (5)$$

According to (5), it can be known that the new space order components $kp\pm1$ and $kp\pm\eta Q_s\pm1$ of the no-load radial magnetic field are introduced because of SE, shown in Table 1.

3 Analytical model of no-load back-EMF

3.1 No-load back-EMF of unit motors and the whole motor without eccentricity

For an ER-PMSM with $2p$ poles and Q_s slots, the whole motor can be divided into GCD(p, Q_s) unit motors, shown in Fig. 3. Based on the analytical model of the no-load radial magnetic field, the analytical model of no-load back-EMF is established. Back-EMF of each conductor in the slot is

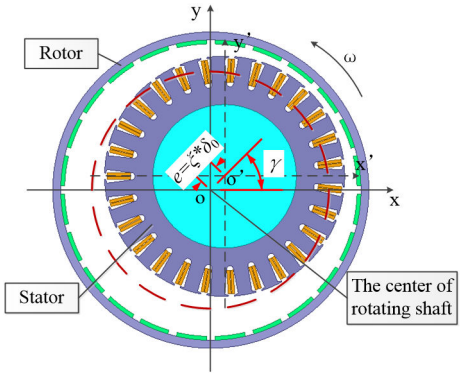

Fig. 2 *Schematic diagram of SE distance e and SE circumferential angle γ*

Table 1 Space order and frequency characteristics of no-load radial magnetic field of ER-PMSM with SE

Source	Space order characteristics	Frequency characteristics
interaction of B_{r-s}, λ_0, ε_0	kp	kf_c
interaction of B_{r-s}, λ_0, $\varepsilon_1\cos(\theta-\gamma)$	$kp\pm1$	kf_c
interaction of B_{r-s}, $\sum_{\eta=1}^{N_\lambda}\lambda_{a\eta}\cos(\eta Q_s\theta)$, ε_0	$kp\pm\eta Q_s$	kf_c
interaction of B_{r-s}, $\sum_{\eta=1}^{N_\lambda}\lambda_{a\eta}\cos(\eta Q_s\theta)$, $\varepsilon_1\cos(\theta-\gamma)$	$kp\pm\eta Q_s\pm1$	kf_c
interaction of B_{t-s}, λ_b, ε_0	$kp\pm\eta Q_s$	kf_c
interaction of B_{t-s}, λ_b, $\varepsilon_1\cos(\theta-\gamma)$	$kp\pm\eta Q_s\pm1$	kf_c

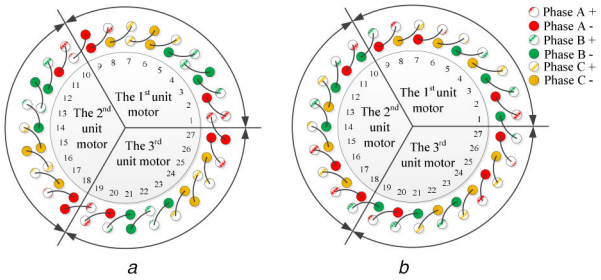

Fig. 3 *Winding distribution diagram of ER-PMSM*
(a) Whole coiled, ***(b)*** Half coiled

$$e_i=N_sL\omega rB_r(R_s,\theta_i,t) \quad (6)$$

where N_s is a number of turns per slot, L is the conductor length, r is the radius of the conductor position, R_s is the outer diameter of stator, $\theta_i=(i-1)\theta_0+\theta_1$ is the angle corresponding to slot i, $\theta_0=2\pi/27$ is the slot-pitch angle.

According to the winding distribution of the motor, the numbers of slots per phase are determined. No-load back-EMF of the whole coiled and half coiled winding distribution modes of the 24-pole-27-slot ER-PMSM are analysed. Their winding distributions are shown in Fig. 3. The number of poles generated by the whole coiled winding is equal to the number of pole-phase groups per phase, while that of poles generated by the half wingding is equal to twice the number of pole-phase groups per phase.

For the whole coiled winding distribution mode in Fig. 4*a*, the slot numbers of phase A, phase B, and phase C are represented as follows:

$$A_w=\{1,2,8,9,10,11,17,18,19,20,26,27\}$$
$$B_w=\{2,3,4,5,11,12,13,14,20,21,22,23\}$$
$$C_w=\{5,6,7,8,14,15,16,17,23,24,25,26\}$$

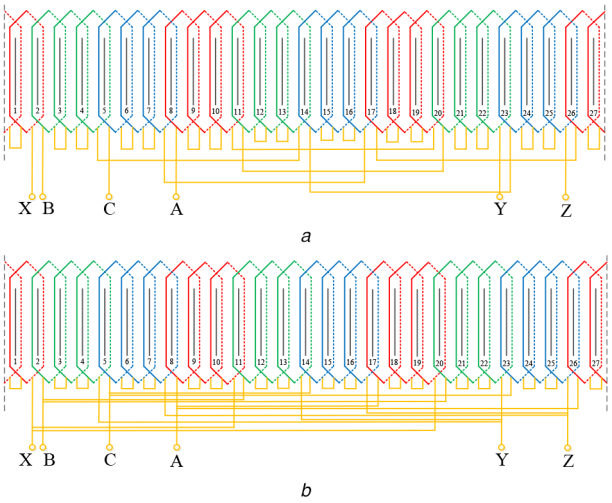

Fig. 4 *Winding connection diagram with different parallel branch numbers of ER-PMSM*
(a) Parallel branch number is 1, ***(b)*** Parallel branch number is 3

For the half-coiled winding distribution mode in Fig. 4*b*, the slot numbers of phase A, phase B, and phase C are, respectively

$$A_{\mathrm{h}} = \{1, 2, 6, 7, 8, 9, 10, 11, 15, 16, 17, 18, 19, 20, 24, 25, 26, 27\}$$
$$B_{\mathrm{h}} = \{1, 2, 3, 4, 5, 9, 10, 11, 12, 13, 14, 18, 19, 20, 21, 22, 23, 27\}$$
$$C_{\mathrm{h}} = \{3, 4, 5, 6, 7, 8, 12, 13, 14, 15, 16, 17, 21, 22, 23, 24, 25, 26\}$$

Since the GCD of pole number 24 and slot number 27 is 3, the parallel branch numbers are 1 and 3, respectively. Therefore, there are two winding connection ways. For example, the winding connection diagram of the whole coiled winding distribution mode is shown in Fig. 4.

If the parallel branch number is equal to 1, three unit motors are in series and no-load back-EMF can be calculated [28, 29]

$$\begin{cases} e_{A\_a1} = \sum\limits_{i \in A} \frac{1}{2} k_i N_{\mathrm{s}} L \omega r B_{\mathrm{r}}(R_{\mathrm{s}}, \theta_i, t) \\ e_{B\_a1} = \sum\limits_{i \in B} \frac{1}{2} k_i N_{\mathrm{s}} L \omega r B_{\mathrm{r}}(R_{\mathrm{s}}, \theta_i, t) \\ e_{C\_a1} = \sum\limits_{i \in C} \frac{1}{2} k_i N_{\mathrm{s}} L \omega r B_{\mathrm{r}}(R_{\mathrm{s}}, \theta_i, t) \end{cases} \tag{7}$$

where, when slot i contains single- or two-phase conductors, $k_i = 2$ or $k_i = 1$, respectively, $i = 1, 2, \ldots, 27$.

If the parallel branch number of the ER-PMSM is equal to 3, three unit motors are in parallel and the amplitude of back-EMF per phase of the whole motor is equal to that of each unit motor. The analytical expressions of no-load back-EMF of the first unit motor are [28, 29]

$$\begin{cases} e_{A_{U1}} = \sum\limits_{i \in A_{U1}} \frac{1}{2} k_i N_{\mathrm{s}} L \omega r B_{\mathrm{r}}(R_{\mathrm{s}}, \theta_i, t) \\ e_{B_{U1}} = \sum\limits_{i \in B_{U1}} \frac{1}{2} k_i N_{\mathrm{s}} L \omega r B_{\mathrm{r}}(R_{\mathrm{s}}, \theta_i, t) \\ e_{C_{U1}} = \sum\limits_{i \in C_{U1}} \frac{1}{2} k_i N_{\mathrm{s}} L \omega r B_{\mathrm{r}}(R_{\mathrm{s}}, \theta_i, t) \end{cases} \tag{8}$$

The no-load back-EMF of the whole motor is calculated through no-load back-EMF of three unit motors

$$\begin{cases} e_{A\_a3} = \frac{1}{3}\left[e_{A_{U1}} + e_{A_{U2}} + e_{A_{U3}}\right] \\ e_{B\_a3} = \frac{1}{3}\left[e_{B_{U1}} + e_{B_{U2}} + e_{B_{U3}}\right] \\ e_{C\_a3} = \frac{1}{3}\left[e_{C_{U1}} + e_{C_{U2}} + e_{C_{U3}}\right] \end{cases} \tag{9}$$

where $e_{A_{U1}}$, $e_{A_{U2}}$, $e_{A_{U3}}$ represent the no-load back-EMF of A-phase of three unit motors, respectively.

3.2 No-load back-EMF of unit motor and whole motor with SE

By substituting the no-load radial magnetic field of ER-PMSM with SE into the analytical expressions of no-load back-EMF of ER-PMSM without eccentricity, the analytical model of no-load back-EMF of ER-PMSM with SE can be obtained similarly.

The analytical model of no-load back-EMF with SE for the unit motor and the whole motor when the number of parallel branches is 1 are shown in (10)

$$\begin{cases} e_{A\_a1-\mathrm{se}} = \sum\limits_{i \in A} \frac{1}{2} k_i N_{\mathrm{s}} L \omega r B_{\mathrm{r-se}}(R_{\mathrm{s}}, \theta_i, t) \\ e_{B\_a1-\mathrm{se}} = \sum\limits_{i \in B} \frac{1}{2} k_i N_{\mathrm{s}} L \omega r B_{\mathrm{r-se}}(R_{\mathrm{s}}, \theta_i, t) \\ e_{C\_a1-\mathrm{se}} = \sum\limits_{i \in C} \frac{1}{2} k_i N_{\mathrm{s}} L \omega r B_{\mathrm{r-se}}(R_{\mathrm{s}}, \theta_i, t) \end{cases} \tag{10}$$

For the case when a number of parallel branches is 3, the no-load back-EMF with SE of the unit motor and the whole motor can be calculated by (11) and (12), separately

$$\begin{cases} e_{A_{U1}-\mathrm{se}} = \sum\limits_{i \in A_{U1}} \frac{1}{2} k_i N_{\mathrm{s}} L \omega r B_{\mathrm{r-se}}(R_{\mathrm{s}}, \theta_i, t) \\ e_{B_{U1}-\mathrm{se}} = \sum\limits_{i \in B_{U1}} \frac{1}{2} k_i N_{\mathrm{s}} L \omega r B_{\mathrm{r-se}}(R_{\mathrm{s}}, \theta_i, t) \\ e_{C_{U1}-\mathrm{se}} = \sum\limits_{i \in C_{U1}} \frac{1}{2} k_i N_{\mathrm{s}} L \omega r B_{\mathrm{r-se}}(R_{\mathrm{s}}, \theta_i, t) \end{cases} \tag{11}$$

$$\begin{cases} e_{A\_a3-\mathrm{se}} = \frac{1}{3}\left[e_{A_{U1}-\mathrm{se}} + e_{A_{U2}-\mathrm{se}} + e_{A_{U3}-\mathrm{se}}\right] \\ e_{B\_a3-\mathrm{se}} = \frac{1}{3}\left[e_{B_{U1}-\mathrm{se}} + e_{B_{U2}-\mathrm{se}} + e_{B_{U3}-\mathrm{se}}\right] \\ e_{C\_a3-\mathrm{se}} = \frac{1}{3}\left[e_{C_{U1}-\mathrm{se}} + e_{C_{U2}-\mathrm{se}} + e_{C_{U3}-\mathrm{se}}\right] \end{cases} \tag{12}$$

4 Verification of analytical model of no-load back-EMF of ER-PMSM without eccentricity and with SE

4.1 FEM and experimental verification of no-load back-EMF of ER-PMSM without eccentricity

To verify the accuracy of the no-load radial magnetic field and no-load back-EMF analytical models, the 24-pole-and-27-slot ER-PMSM with the whole coiled winding distribution mode is taken as an example to carry out relevant verification. The main parameters of the motor are listed in Table 2. Its mesh model, presenting the greater number of nodes in the air gap, is shown in Fig. 5.

The no-load back-EMF of ER-PMSM can be measured through the generator method. The test rig sketch is shown in Fig. 6. The electric dynamometer (dyno), and torque and speed sensor are connected with the motor. The ER-PMSM is dragged by the dyno as a generator under no-load at rated speed (600 rpm). The three-phase voltages are measured and they are equal to the no-load back-EMF of phase A, phase B, and phase C.

The analytical, FEM, and experimental results of no-load back-EMF of ER-PMSM are compared in Fig. 7. The root mean square errors (RMSEs) are evaluated as well in Table 3. According to

Table 2 Main parameters of ER-PMSM

Parameter	Symbol	Value	Unit
number of pole-pairs	p	12	—
number of slots	Q_s	27	—
number of turns per slot	N_s	15	—
radius of stator outer surface	R_s	123.2	mm
radius of rotor inner surface	R_r	128.2	mm
air-gap length	g	1.00	mm
axial length	L	35	mm
residual magnetic intensity	B_r	1.045	T

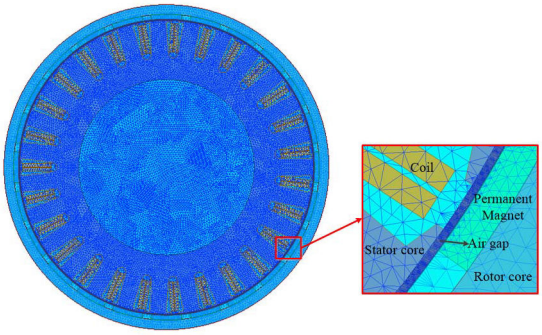

Fig. 5 *Mesh model of ER-PMSM*

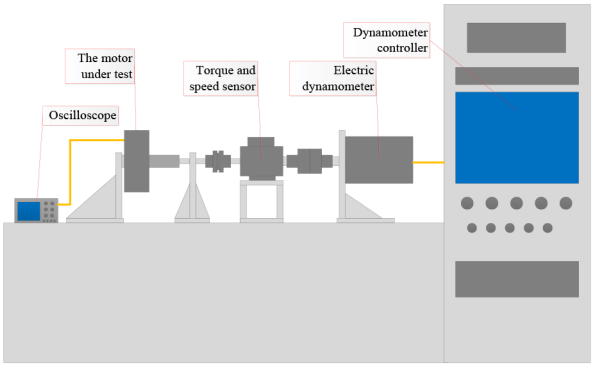

Fig. 6 *Experimental rig of no-load back-EMF*

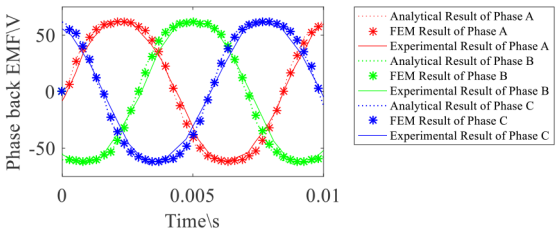

Fig. 7 *Analytical, FEM and experimental results of no-load back-EMF without eccentricity*

Fig. 7 and Table 3, the analytical, FEM, and experimental results are in good agreement.

4.2 FEM verification of no-load back-EMF of ER-PMSM with SE

The analytical and FEM results of no-load back-EMF of ER-PMSM at the eccentric position, of which the SE ratio and SE circumferential angle are 60% and 60°, respectively, are compared in Fig. 8. Owing to the limitation of experimental conditions, the analytical results of no-load back-EMF of ER-PMSM with SE are not verified by the experiment. The RMSE between analytical and FEM results of phase A, phase B, and phase C are 3.149, 4.420, and 4.468, respectively. Therefore, it can be concluded that the analytical results of no-load back-EMF of ER-PMSM with SE are

Table 3 RMSE of analytical, FEM and experimental results of no-load Back-EMF of ER-PMSM without eccentricity

Phase	Analytical and FEM results	Analytical and experimental results	FEM and experimental results
phase A	2.495	6.074	4.610
phase B	3.888	5.856	5.814
phase C	4.011	5.933	5.228

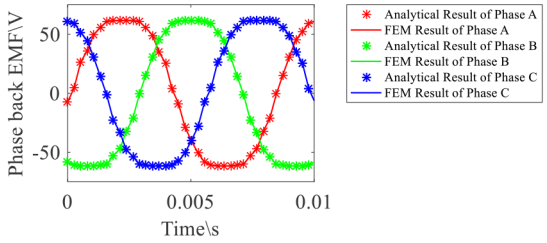

Fig. 8 *Analytical and FEM results of no-load back-EMF of ER-PMSM with SE (SE ratio 60%, SE circumferential angle 60°)*

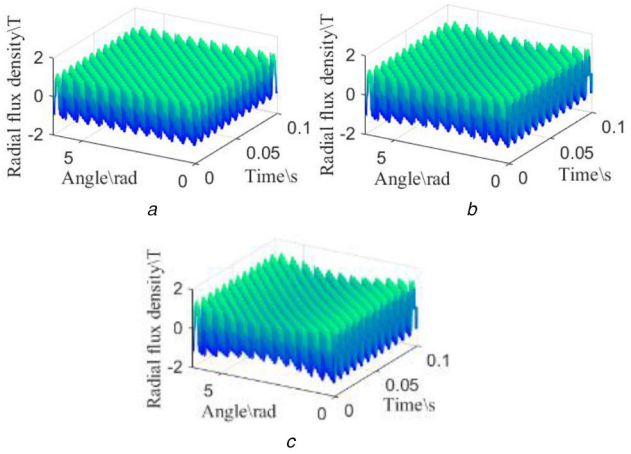

Fig. 9 *No-load radial magnetic field of ER-PMSM with different SE ratios* ***(a)*** $\xi = 0\%$, ***(b)*** $\xi = 45\%$, ***(c)*** $\xi = 90\%$

in good agreement with FEM results and the accuracy of the proposed analytical model is verified.

5 Effects of SE positions on no-load back-EMF of ER-PMSM

5.1 No-load radial magnetic field of ER-PMSM with different SE ratios

Different SE ratios lead to different changes in air gap length of ER-PMSM and then affect the no-load radial magnetic field. Under the same SE circumferential angle 0°, no-load radial magnetic field of ER-PMSM with different SE ratios is analysed in Fig. 9. On the one hand, when ER-PMSM is not eccentric, the local maximum amplitudes of the no-load radial magnetic field do not change with time and space angle. On the other hand, when it is under SE, the local maximum amplitudes of the no-load magnetic field do not change with time, but first decrease and then increase with space angle. Additionally, changes in the local maximum amplitudes increase with the increasing SE ratios. When the stator is offset by a certain distance on a complete circumference, the shortest air gap length and the longest air gap length are separated by half a circumference. Since the permeance at the air gap is much smaller than that of the stator core and rotor core, the magnetic field amplitude at the shortest air gap is the largest. The larger the SE ratio, the longer the stator deviation distance. Then it causes a larger change of local maximum amplitudes of the no-load magnetic field.

Two-dimensional Fourier transform results of the no-load radial magnetic field of ER-PMSM with different SE ratios are shown in

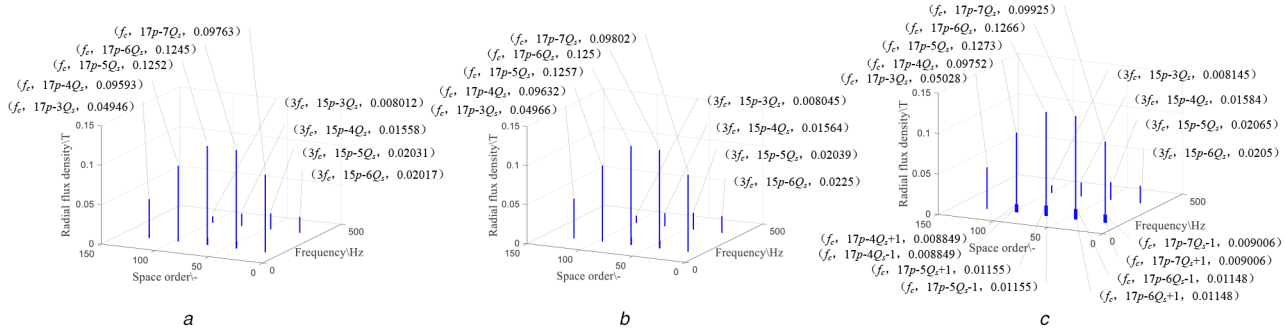

Fig. 10 *Two-dimensional Fourier transform results of the no-load radial magnetic field of ER-PMSM with different SE ratios*
(a) $\xi = 0\%$, ***(b)*** $\xi = 45\%$, ***(c)*** $\xi = 90\%$

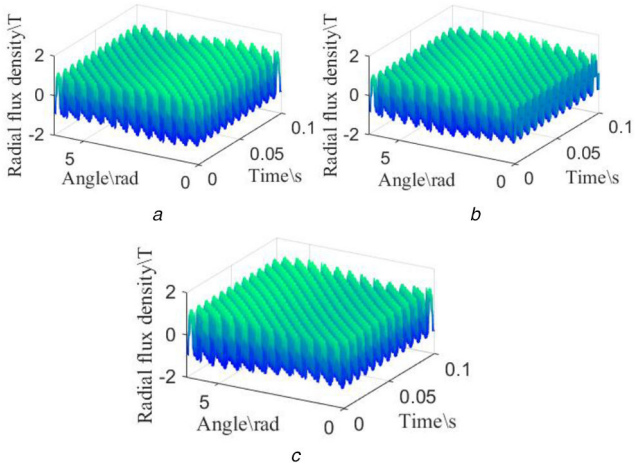

Fig. 11 *No-load radial magnetic field of with different SE circumferential angles*
(a) $\gamma = 90°$, ***(b)*** $\gamma = 180°$, ***(c)*** $\gamma = 270°$

Fig. 10. The frequency characteristics of the no-load radial magnetic field are not affected by SE ratios. However, new space order components $kp \pm 1$ and $kp \pm \eta Q_s \pm 1$ of the no-load radial magnetic field are introduced because of SE, which have been predicted in Table 1. The new space order components $kp \pm 1$ and $kp \pm \eta Q_s \pm 1$ are side-band components of space order kp and $kp \pm \eta Q_s$, respectively. In addition, their amplitudes increase with the increasing SE ratio.

5.2 No-load radial magnetic field of ER-PMSM with different SE circumferential angles

Under the same SE ratio 60%, the effects of different SE circumferential angles on the no-load radial magnetic field are compared in Fig. 11. No-load radial magnetic field presents obvious fluctuation changes with the change of the SE circumferential angle. Its reason is that the variation of the SE circumferential angle leads to the position change of the shortest air gap along the complete circumference. It leads to the position change of the largest amplitude of the no-load air gap magnetic field along the space angle further.

5.3 No-load back-EMF of each unit motor with different SE positions

Based on the no-load back-EMF analytical model, the effects of different SE ratios and different SE circumferential angles on no-load back-EMF of each unit motor are analysed in Fig. 12. With the increasing SE ratio and SE circumferential angle, the amplitudes of no-load back-EMF of each phase of a unit motor increase continuously but are asymmetric. In other words, SE distorts no-load back-EMF of each unit motor.

Stator winding configurations greatly affect the back-EMF spectra [30]. To evaluate the distortion degree of three-phase back-

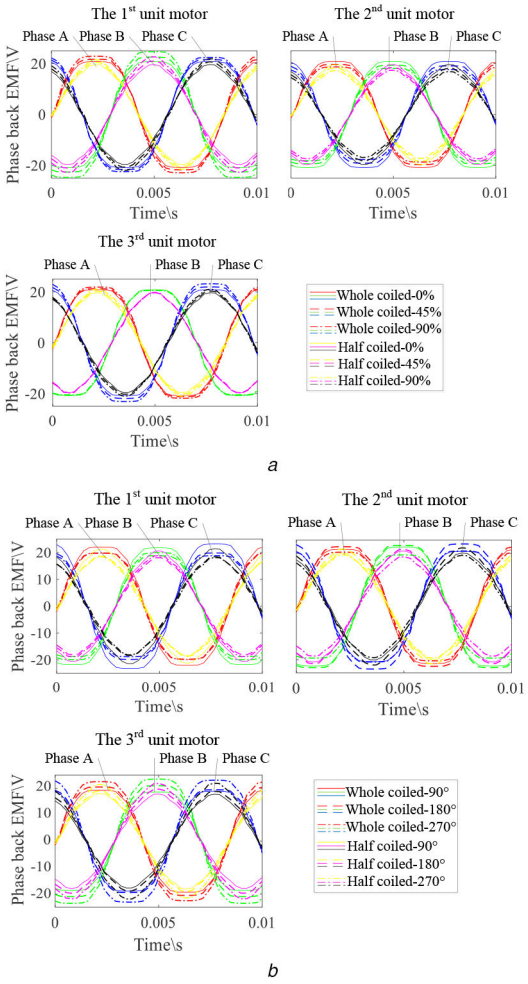

Fig. 12 *Comparison of no-load back-EMF of unit motors with different SE positions*
(a) With different SE ratios, ***(b)*** With different SE circumferential angles

EMF more intuitively, total harmonic distortion (THD) is used as an index

$$\mathrm{THD}_{i\_m}(\xi,\gamma) = \frac{e_{i\_m}(\xi,\gamma) - e'_{i\_m}(\xi,\gamma)}{e'_{i\_m}(\xi,\gamma)} \times 100\% \tag{13}$$

where i is the number of unit motor and m is the phase of back-EMF. When comparing no-load back-EMF with different SE ratios and a certain SE circumferential angle, $e_{i\_m}(\xi, \gamma)$ is the no-load back-EMF amplitude with different SE ratios, $e'_{i\_m}(\xi,\gamma)$ is the no-load back-EMF amplitude of the corresponding phase in the corresponding unit motor when the SE ratio is 0%. When comparing no-load back-EMF with different SE circumferential angles and a certain SE ratio, $e_{i\_m}(\xi, \gamma)$ is the no-load back-EMF amplitude at different SE circumferential angles, $e'_{i\_m}(\xi,\gamma)$ is the

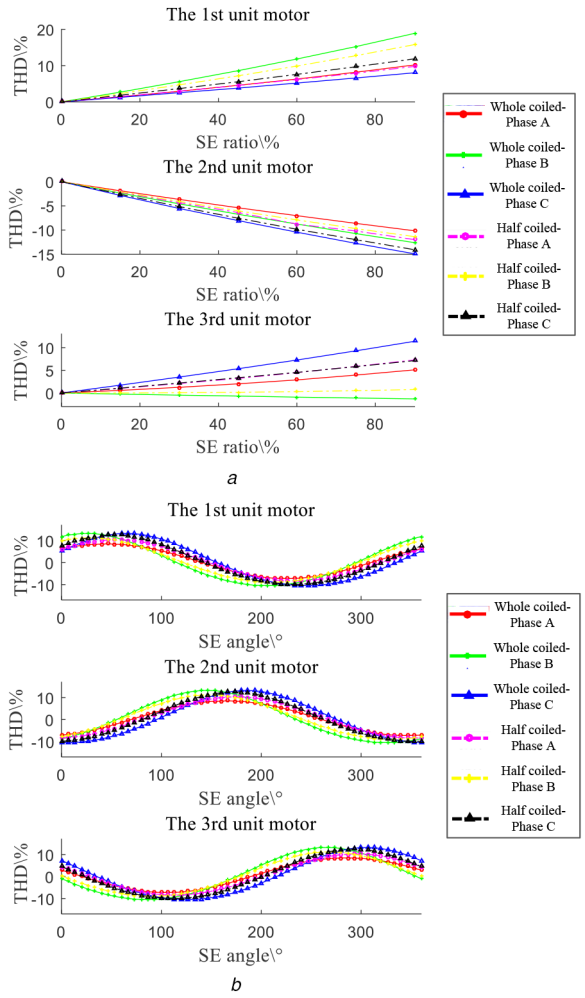

Fig. 13 *Comparison of THD of no-load back-EMF of each unit motor with different SE positions*

(a) With different SE ratios, ***(b)*** With different SE circumferential angles

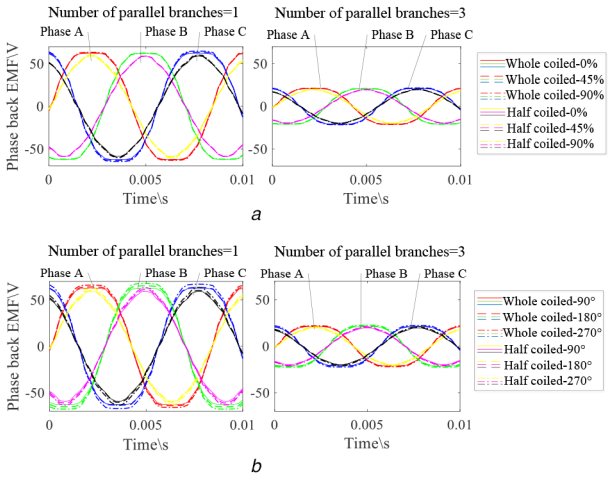

Fig. 14 *Comparison of no-load back-EMF of the whole motor with different SE positions*

(a) With different SE ratios, ***(b)*** With different SE circumferential angles

no-load back-EMF amplitude of the corresponding phase in the corresponding unit motor when the SE circumferential angle is 0°.

A comparison of THD of no-load back-EMF of each unit motor at different SE positions is shown in Fig. 13. On the one hand, the THD of the three-phase no-load back-EMF of each unit motor increases or decreases monotonously with the increasing SE ratio. On the other hand, all the THDs of three-phase no-load back-EMF of each unit motor present a sinusoidal trend with the increasing SE circumferential angle, and their period is a whole circumference.

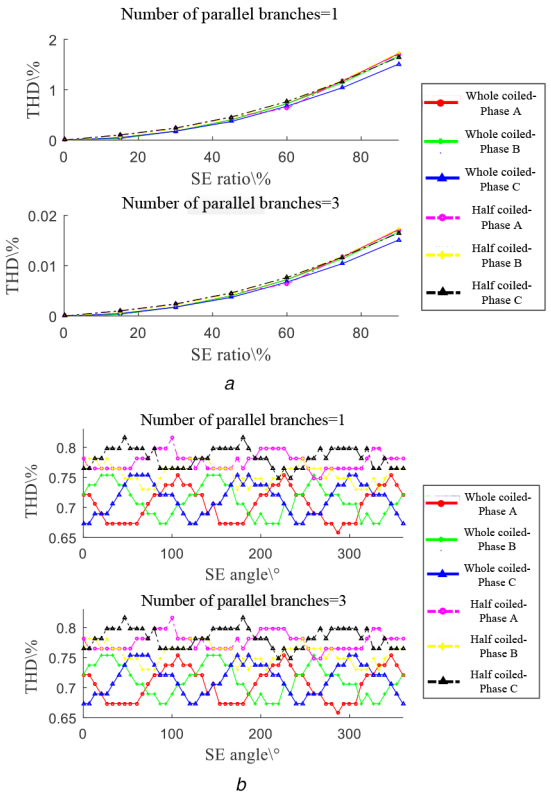

Fig. 15 *Comparison of THD of no-load back-EMF of the whole motor with different SE positions*

(a) With different SE ratios, ***(b)*** With different SE circumferential angles

By comparing THD curves of three-phase no-load back-EMF of the same unit motor, phase C lags behind phase A, phase A lags behind phase B, and the amplitude of phase A is less than phase B and phase C. By comparing THD curves of no-load back-EMF of the corresponding phase of three unit motors, the second unit motor lags behind the first unit motor by phase angle $2\pi/3$, the third unit motor lags behind the second unit motor by phase angle $2\pi/3$, and the amplitudes of the corresponding phase of three unit motors are the same. Owing to different positions of conductors under the whole coiled and half coiled winding distribution mode, THD curves of no-load back-EMF of each phase of unit motors are not completely consistent, but their overall variation trends are the same.

5.4 No-load back-EMF of whole motor with different SE positions

Based on the no-load Back-EMF analytical model, the effects of different SE ratios and different SE circumferential angles on no-load back-EMF of the whole motor are analysed in Fig. 14. SE has no significant impact on the no-load phase back-EMF of the whole motor for two kinds of parallel branches.

According to (13), THD of three-phase no-load back-EMF of the whole motor with different SE ratios and SE circumferential angles are calculated in Fig. 15. When ER-PMSM with 24 poles/27 slots occurs SE fault, THD curves of three-phase no-load back-EMF of the whole motor have almost the same change trend, and the change range is very small.

If the parallel branch number is equal to 1, three unit motors are in series. Hence, the no-load back-EMF of the whole motor can be calculated by adding no-load back-EMF of conductors in the corresponding slots of each unit motor. When the resultant space orders are $kp \pm 1$, its formula is obtained as

(see (14))

where N is the number of unit motors. When the resultant space orders are $kp \pm \eta Q_s \pm 1$, its formula is shown as (see (15)) . Based on (14) and (15), new space order components $kp \pm 1$ and $kp \pm \eta Q_s \pm 1$ are offset when the magnetic fields generated by conductors in

$$
\begin{aligned}
B_{\mathrm{r-s\_k}}(\theta,r,t) &= \left\{\left\{B_{\mathrm{r-s\_amp\_k}}(r)\times\cos[kp(\theta-\omega t-\theta_0)]\right\}\times\lambda_0\right\}\times[\varepsilon_1\cos(\theta)] \\
&\quad+\left\{\left\{B_{r-\mathrm{s\_amp\_k}}(r)\times\cos\left[kp(\theta-\omega t-\theta_0)+kp\times\frac{1}{N}\times2\pi\right]\right\}\times\lambda_0\right\}\times\left[\varepsilon_1\cos\left(\theta+\frac{1}{N}\times2\pi\right)\right] \\
&\quad+\left\{\left\{B_{\mathrm{r-s\_amp\_k}}(r)\times\cos\left[kp(\theta-\omega t-\theta_0)+kp\times\frac{2}{N}\times2\pi\right]\right\}\times\lambda_0\right\}\times\left[\varepsilon_1\cos\left(\theta+\frac{2}{N}\times2\pi\right)\right] \\
&\quad+\cdots+ \\
&\quad+\left\{\left\{B_{\mathrm{r-s\_amp\_k}}(r)\times\cos\left[kp(\theta-\omega t-\theta_0)+kp\times\frac{N-1}{N}\times2\pi\right]\right\}\times\lambda_0\right\}\times\left[\varepsilon_1\cos\left(\theta+\frac{N-1}{N}\times2\pi\right)\right] \\
&= N\times\left\{\left\{B_{\mathrm{r-s\_amp\_k}}(r)\times\cos[kp(\theta-\omega t-\theta_0)]\right\}\times\lambda_0\right\}\times0 \\
&= 0
\end{aligned}
\tag{14}
$$

$$
\begin{aligned}
B_{\mathrm{r-s\_k}}(\theta,r,t) &= \left\{\left\{B_{\mathrm{r-s\_amp\_k}}(r)\times\cos[kp(\theta-\omega t-\theta_0)]\right\}\times\left[\lambda_{a\eta}\cos(\eta Q\theta)\right]\right\}\times[\varepsilon_1\cos(\theta)] \\
&\quad+\left\{\left\{B_{\mathrm{r-s\_amp\_k}}(r)\times\cos\left[kp(\theta-\omega t-\theta_0)+kp\times\frac{1}{N}\times2\pi\right]\right\}\times\left[\lambda_{a\eta}\cos\left(\eta Q\theta+\eta Q\times\frac{1}{N}\times2\pi\right)\right]\right\} \\
&\qquad\times\left[\varepsilon_1\cos\left(\theta+\frac{1}{N}\times2\pi\right)\right] \\
&\quad+\left\{\left\{B_{\mathrm{r-s\_amp\_k}}(r)\times\cos\left[kp(\theta-\omega t-\theta_0)+kp\times\frac{2}{N}\times2\pi\right]\right\}\times\left[\lambda_{a\eta}\cos\left(\eta Q\theta+\eta Q\times\frac{2}{N}\times2\pi\right)\right]\right\} \\
&\qquad\times\left[\varepsilon_1\cos\left(\theta+\frac{2}{N}\times2\pi\right)\right] \\
&\quad+\cdots+ \\
&\quad+\left\{\left\{B_{\mathrm{r-s\_amp\_k}}(r)\times\cos\left[kp(\theta-\omega t-\theta_0)+kp\times\frac{N-1}{N}\times2\pi\right]\right\}\times\left[\lambda_{a\eta}\cos\left(\eta Q\theta+\eta Q\times\frac{N-1}{N}\times2\pi\right)\right]\right\} \\
&\qquad\times\left[\varepsilon_1\cos\left(\theta+\frac{N-1}{N}\times2\pi\right)\right] \\
&= N\times\left\{\left\{B_{\mathrm{r-s\_amp\_k}}(r)\times\cos[kp(\theta-\omega t-\theta_0)]\right\}\times\left[\lambda_{a\eta}\cos(\eta Q\theta)\right]\right\}\times0 \\
&= 0
\end{aligned}
\tag{15}
$$

the corresponding slots are added. In other words, SE has no significant effect on the no-load back-EMF of the whole motor.

If the parallel branch number is equal to 3, three unit motors are in parallel. Hence, the branch of each unit motor can be equivalent to the series connection of a voltage source and a winding resistance. SE leads to different voltages on each branch, and a circulation generates because of the voltage difference between the branches. Voltages on the three branches after balancing are equal to each other, and the final output voltage in parallel is equal to that without SE.

6 Eccentric position diagnosis of SE fault

The in-wheel motor has two main modes: the driving mode as a motor and the regenerative braking mode as a generator.

(i) When the in-wheel motor is under the driving mode, the phase currents modulated by pulse-width modulation contain a large number of harmonics. Harmonic currents lead to the existence of harmonics in back-EMF, resulting in serious distortion of back-EMF. The influences of the SE ratio and SE circumferential angle on back-EMF under load are no longer regular in this case. Hence, back-EMF under load cannot be used as the detection index of SE fault.

(ii) When the in-wheel motor is under the regenerative braking mode, it is dragged forward by the wheel because of the inertia. Then the in-wheel motor is operating as a generator to charge the battery in this case. The effects of the SE ratio and SE circumferential angle on no-load back-EMF show strong regularity. In addition, the motor speed changes slowly after a power failure, and the decrease time of speed is far more than the change period of back-EMF [2]. As a result, it can be approximated to a steady state at the moment of initial braking. The voltage generated by the winding during this period can be approximated to no-load back-EMF. From the above, no-load back-EMF can be used as the detection index of SE fault.

As a result, no-load back-EMF has practical engineering significance as the detection index of SE fault of ER-PMSM.

6.1 Diagnostic criteria

According to the above calculation and analysis, SE does not affect no-load back-EMF of the whole motor for rotary symmetric motor but affects no-load back-EMF of each unit motor. Therefore, no-load back-EMF of unit motor can be used as a criterion to diagnose whether the motor occurs SE. Based on the previous sections, with the increase of SE ratio, the variation curve of THD of no-load back-EMF shows a monotonic growth or a monotonic decline trend under the same SE circumferential angle. With the increase of the SE circumferential angle, the variation curve of THD of no-load back-EMF shows a sinusoidal change trend under the same SE ratio. Additionally, the THD curves of three unit motors are not consistent. Hence, the SE ratio and SE circumferential angle can be uniquely determined through THD of no-load back-EMF of three unit motors when the SE fault occurs. To calculate THD of no-load back-EMF of unit motors with different SE ratios and SE circumferential angles, six levels of SE ratios (15, 30, 45, 60, 75, and 90%) and 55 levels of circumferential angles (0, α_0, $2\alpha_0$, $3\alpha_0$, $4\alpha_0$,…, $54\alpha_0$, where α_0 is half of the slot pitch angle) are considered. In Fig. 16, the centre point of the circle is the rotor centre (the rotating centre), and these '×' stand for possible eccentric positions of the stator centre considered in this paper. Their total number is 330.

6.2 Diagnostic method

The projection method of intersection lines is proposed to diagnose the eccentric position of ER-PMSM with SE fault. Firstly, no-load back-EMF of unit motors should be measured. If the unit motor number of the whole motor is equal to 1, directly measure the three-phase no-load back-EMF of the whole motor. If the unit motor number is >1, measure the three-phase no-load back-EMF of each unit motor through the outgoing wire. Then, according to the

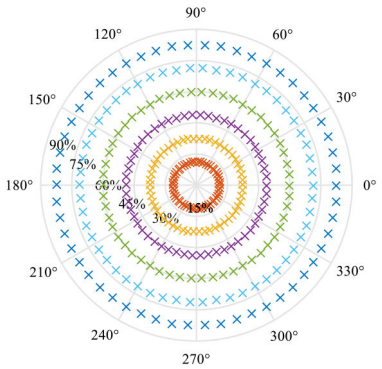

Fig. 16 *Possible eccentric positions of the stator centre considered in this paper*

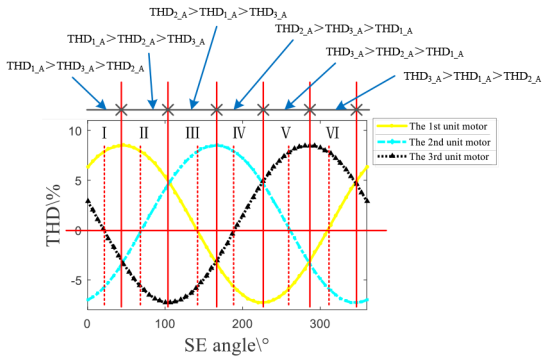

Fig. 17 *Variation of THD of no-load back-EMF with SE circumferential angles*

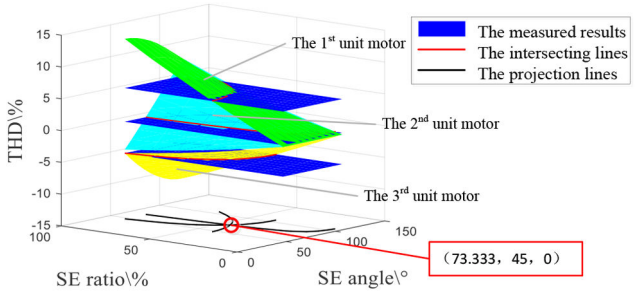

Fig. 18 *THD curve of no-load back-EMF of phase A of three unit motors with different SE positions*

measured no-load back-EMF of unit motors, THD should be calculated, respectively, according to (10). By comparing THD of the corresponding phases of three unit motors, the range of SE circumferential angle is roughly determined. The THD curves of no-load back-EMF of phase A of the three unit motors in Fig. 13*b* are placed on the same circumference for comparison, as shown in Fig. 17. Taking the whole coiled winding distribution mode as an example, the phase of the THD curve of three-phase no-load back-EMF varying with SE circumferential angle of each unit motor does not change with the SE ratio. The THD curve within a period can be divided into different regions. A period is divided into six segments by taking the intersection of the corresponding THD curves of three unit motors as the boundary. The relative magnitudes of THD of three unit motors in each segment are all different, and three curves in each segment change monotonously, as shown in the red solid line in Fig. 17. Furthermore, according to the positive and negative THD of one unit motor, the range of the SE circumferential angle can be located into smaller ones, as shown in the red dotted line in Fig. 17. Finally, according to the actual measured THD of no-load back-EMF of each unit motor, the possible SE ratios and corresponding SE circumferential angles of each unit motor can be determined. The SE ratio and SE circumferential angle of the whole motor can be determined through their coincidence point.

A SE fault with SE ratio 45% and SE circumferential angle 73.333° is taken as an example to illustrate. In this case, THDs of measured no-load back-EMF of phase A are 5.580, 0.289, and −4.668, respectively. The SE circumferential angle can be determined in II of Fig. 17 through these THDs. Draw the surface of THD varying with SE ratios in the range of SE circumferential angles in II. Then, the three measured THD values are extended into three planes. These three planes generate three intersecting lines with the three THD surfaces, respectively, which is the possible SE positions of the three unit motors under these THD values. Finally, the three intersecting lines are projected onto the *xy* plane, i.e. the three intersecting lines are intersected. The intersection points are its SE ratio and SE circumferential angle of the whole motor in Fig. 18.

7 Conclusion

A projection method of intersection lines is proposed to diagnose the eccentric position of SE fault of ER-PMSM used as an in-wheel motor. The main conclusions are as follows:

(i) The frequency characteristics of the no-load radial magnetic field are not affected by SE ratios. However, new space order components $kp \pm 1$ and $kp \pm \eta Q_s \pm 1$ of the no-load radial magnetic field are introduced because of SE. The new space order components $kp \pm 1$ and $kp \pm \eta Q_s \pm 1$ are side-band components of space order kp and $kp \pm \eta Q_s$, respectively. In addition, their amplitudes increase with the increasing SE ratio.

(ii) For the unit motor of ER-PMSM, SE causes the distortion of the three-phase no-load back-EMF no matter the windings are distributed in whole coiled mode or half coiled mode. The degree of distortion increases with the increasing SE ratio. The THD curve presents a sinusoidal change trend with the increasing SE circumferential angle. For ER-PMSM with a unit motor number >1, SE does not affect no-load back-EMF of the whole motor.

(iii) This eccentric position diagnosis method does not need to add certain additional devices to ER-PMSM. In addition, both the SE ratio and SE circumferential angle can be diagnosed meanwhile. This method is effective, direct, and inexpensive.

8 References

[1] Yang, Y., Rahman, M.M., Lambert, T., *et al.*: 'Development of an external rotor V-shape permanent magnet machine for E-bike application', *IEEE Trans. Energy Convers.*, 2018, **33**, (4), pp. 1650–1658

[2] Yang, Y.B., Chen, J., Yan, B., *et al.*: 'Analytical magnetic field prediction of flux switching machine with segmental rotor', *IET Electr. Power Appl.*, 2019, **13**, (1), pp. 91–100

[3] Yang, Y.B., Wang, X.H., Zhang, Z.S.: 'Analytical calculation of magnetic field and electromagnetic performance of flux reversal machines', *IET Electr. Power Appl.*, 2014, **8**, (5), pp. 178–188

[4] Zhu, Z.Q., Wu, L.J., Xia, Z.P.: 'An accurate subdomain model for magnetic field computation in slotted surface-mounted permanent-magnet machines', *IEEE Trans. Magn.*, 2010, **46**, (4), pp. 1100–1115

[5] Rahideh, A., Korakianitis, T.: 'Analytical calculation of open-circuit magnetic field distribution of slotless brushless PM machines', *Int. J. Electr. Power Energy Syst.*, 2013, **44**, (1), pp. 99–114

[6] Moayed-Jahromi, H., Rahideh, A., Mardaneh, M.: '2-D analytical model for external rotor brushless PM machines', *IEEE Trans. Energy Convers.*, 2016, **31**, (3), pp. 1100–1109

[7] Hu, H.Z., Zhao, J., Liu, X.D., *et al.*: 'No-load magnetic field and cogging force calculation in linear permanent-magnet synchronous machines with semiclosed slots', *IEEE Trans. Ind. Electron.*, 2017, **64**, (7), pp. 5564–5575

[8] Liang, P.X., Chai, F., Li, Y., *et al.*: 'Analytical prediction of magnetic field distribution in spoke-type permanent-magnet synchronous machines accounting for bridge saturation and magnet shape', *IEEE Trans. Ind. Electron.*, 2017, **64**, (5), pp. 3479–3488

[9] Pourahmadi-Nakhli, M., Rahideh, A., Mardaneh, M.: 'Analytical 2-D model of slotted brushless machines with cubic spoke-type permanent magnets', *IEEE Trans. Energy Convers.*, 2018, **33**, (1), pp. 373–382

[10] Zhou, Y., Li, H.S., Meng, G.W., *et al.*: 'Analytical calculation of magnetic field and cogging torque in surface-mounted permanent magnet machines accounting for any eccentric rotor shape', *IEEE Trans. Ind. Electron.*, 2015, **62**, (6), pp. 3438–3447

[11] Zarko, D., Ban, D., Lipo, T.A.: 'Analytical calculation of magnetic field distribution in the slotted air gap of a surface permanent-magnet motor using complex relative air-gap permeance', *IEEE Trans. Magn.*, 2006, **42**, (7), pp. 1828–1837

[12] Ma, C.G., Chen, C.Y., Li, Q., *et al.*: 'Analytical calculation of no-load magnetic field of external rotor permanent magnet brushless direct current motor used as in-wheel motor of electric vehicle', *IEEE Trans. Magn.*, 2018, **54**, (4), pp. 1–6
[13] Park, H., Woo, D., Jung, S., *et al.*: 'Modeling and analysis of magnet skew in axial flux permanent-magnet motor via field reconstruction method'. 19th Int. Conf. on Electrical Machines and Systems (ICEMS), Chiba, Japan, 2016
[14] Rahideh, A., Korakianitis, T.: 'Analytical magnetic field distribution of slotless brushless machines with inset permanent magnets', *IEEE Trans. Magn.*, 2011, **47**, (6), pp. 1763–1774
[15] Rahideh, A., Mardaneh, M., Korakianitis, T.: 'Analytical 2-D calculations of torque, inductance, and back-EMF for brushless slotless machines with surface inset magnets', *IEEE Trans. Magn.*, 2013, **49**, (8), pp. 4873–4884
[16] Kim, U., Lieu, D.K.: 'Magnetic field calculation in permanent magnet motors with rotor eccentricity: without slotting effect', *IEEE Trans. Magn.*, 1998, **34**, (4), pp. 2243–2252
[17] Kim, U., Lieu, D.K.: 'Magnetic field calculation in permanent magnet motors with rotor eccentricity: with slotting effect considered', *IEEE Trans. Magn.*, 1998, **34**, (4), pp. 2253–2266
[18] Jalali, P., Boroujeni, S.T., Bianchi, N.: 'Simple and efficient model for slotless eccentric surface-mounted PM machines', *IET Electr. Power Appl.*, 2017, **11**, (4), pp. 631–639
[19] Rahideh, A., Korakianitis, T.: 'Analytical open-circuit magnetic field distribution of slotless brushless permanent-magnet machines with rotor eccentricity', *IEEE Trans. Magn.*, 2011, **47**, (12), pp. 4791–4808
[20] Zhu, Z.Q., Wu, L.J., Mohd Jamil, M.L.: 'Distortion of back-EMF and torque of PM brushless machines due to eccentricity', *IEEE Trans. Magn.*, 2013, **49**, (8), pp. 4927–4936
[21] Zheng, M., Zhu, Z.Q., Cai, S., *et al.*: 'Influence of magnetic saturation and rotor eccentricity on back EMF of novel hybrid-excited stator slot opening permanent magnet machine', *IEEE Trans. Magn.*, 2018, **54**, (11), pp. 1–5
[22] Ebrahimi, B.M., Faiz, J., Roshtkhari, M.J.: 'Static-, dynamic-, and mixed-eccentricity fault diagnoses in permanent-magnet synchronous motors', *IEEE Trans. Ind. Electron.*, 2009, **56**, (11), pp. 4727–4739
[23] Hassanzadeh, M., Faiz, J., Kiyoumarsi, A.: 'A new analytical technique for analysis and detection of air-gap eccentricity fault in surface-mounted permanent-magnet machines', *Int. Trans. Electr. Energy*, 2019, **29**, (3), pp. 1–25
[24] Bessous, N., Zouzou, S.E., Sbaa, S., *et al.*: 'New vision about the overlap frequencies in the MCSA-FFT technique to diagnose the eccentricity fault in the induction motors'. 5th Int. Conf. on Electrical Engineering – Boumerdes (ICEE-B), Boumerdes, Algeria, 2017
[25] Kang, K., Song, J., Kang, C., *et al.*: 'Real-time detection of the dynamic eccentricity in permanent-magnet synchronous motors by monitoring speed and back EMF induced in an additional winding', *IEEE Trans. Ind. Electron.*, 2017, **64**, (9), pp. 7191–7200
[26] Park, Y., Fernandez, D., Lee, S.B., *et al.*: 'Online detection of rotor eccentricity and demagnetization faults in PMSMs based on hall-effect field sensor measurements', *IEEE Trans. Ind. Appl.*, 2019, **55**, (3), pp. 2499–2509
[27] Dorrell, D.G., Salah, A.: 'Detection of rotor eccentricity in wound rotor induction machines using pole-specific search coils', *IEEE Trans. Magn.*, 2015, **51**, (11), pp. 1–4
[28] Ma, C.G., Li, Q.Y., Zheng, P., *et al.*: 'Effects of static eccentricity on the no-load back electromotive force of external rotor permanent magnet brushless DC motor used as in-wheel motor', *IET Electr. Power Appl.*, 2019, **13**, (5), pp. 604–613
[29] Ruschetti, C., Verucchi, C., Bossio, G., *et al.*: 'Rotor demagnetization effects on permanent magnet synchronous machines', *Energy Convers. Manage.*, 2013, **74**, (10), pp. 1–8
[30] Saavedra, H., Urresty, J.C., Riba, J.R., *et al.*: 'Detection of interturn faults in PMSMs with different winding configurations', *Energy Convers. Manage.*, 2014, **79**, (3), pp. 534–542